Aeroelastic deformation of a perforated strip

M. Guttag and H. H. Karimi
Department of Mechanical Engineering, Massachusetts Institute of Technology, Cambridge, Massachusetts 02139, USA

C. Falcón
Departamento de Física, Facultad de Ciencias Físicas y Matemáticas, Universidad de Chile, Casilla 487-3, Santiago, Chile
and Department of Civil and Environmental Engineering, Massachusetts Institute of Technology, Cambridge, Massachusetts 02139, USA

P. M. Reis*
Department of Mechanical Engineering and Department of Civil and Environmental Engineering, Massachusetts Institute of Technology, Cambridge, Massachusetts 02139, USA
and Flexible Structures Laboratory, Ecole Polytechnique Fédérale de Lausanne, 1015 Lausanne, Switzerland

(Received 18 July 2017; published 22 January 2018)

We perform a combined experimental and numerical investigation into the static deformation of perforated elastic strips under uniform aerodynamic loading at high-Reynolds-number conditions. The static shape of the porous strips, clamped either horizontally or vertically, is quantified as they are deformed by wind loading, induced by a horizontal flow. The experimental profiles are compared to numerical simulations using a reduced model that takes into account the normal drag force on the deformed surface. For both configurations (vertical and horizontal clamping), we compute the drag coefficient of the strip, by fitting the experimental data to the model, and find that it decreases as a function of porosity. Surprisingly, we find that, for every value of porosity, the drag coefficients for the horizontal configuration are larger than those of the vertical configuration. For all data in both configurations, with the exception of the continuous strip clamped vertically, a linear relation is found between the porosity and drag. Making use of this linearity, we can rescale the drag coefficient in a way that it becomes constant as a function of the Cauchy number, which relates the force due to fluid loading on the elastic strip to its bending rigidity, independently of the material properties and porosity of the strip and the flow speed. Our findings on flexible strips are contrasted to previous work on rigid perforated plates. These results highlight some open questions regarding the usage of reduced models to describe the deformation of flexible structures subjected to aerodynamic loading.

DOI: 10.1103/PhysRevFluids.3.014003

I. INTRODUCTION

Flexible bodies can be readily deformed by aerodynamic or hydrodynamic loading, and studying the underlying fluid-structure interactions (FSIs) is a topic of intense research [1]. To name just a few representative examples, FSI is prevalent in wide ranging areas including drag reduction in fish locomotion [2], high-speed printing on paper [3], aerodynamic instability of bridges [4–8], energy

*pedro.reis@epfl.ch

harvesting in wind-loaded flexible structures [9–11], the modeling of parachutes [12], the waving of flags and banners [13–15], and the dynamics of wind-loaded flexible wings [16–18]. In classic efforts to model FSI problems, it is common to simplify the underlying flexible object to continuous and smooth structural elements [19,20]. In nature, however, flexible structures exposed to flows are usually not smooth, but rather wrinkled, rough, or even porous [21–23]. For instance, the wings of some insects are flexible porous structures whose porosity has been shown to reduce drag and increase aerodynamic efficiency [23]. Thus, porosity can significantly affect the interaction between a flexible structure and the surrounding flow. In the present study, towards gaining physical understanding of fluid-structure interactions when porosity is taken into account, we consider the static deformation of a flexible perforated strip exposed to uniform air flow.

Let us first focus on FSI problems of continuous (nonporous) flexible structures. The reconfiguration of plant leaves under wind loading is a representative and pedagogical example of such a FSI problem: The self-adaptation of the shape of the leaf at different flow conditions relaxes the state of stress in the plant and reduces the possibility of damage such as uprooting [24]. The wind loading effect can be quantified by measuring the drag force F_d acting on the plant leaves. For bluff bodies exposed to an air flow, the drag force can be written as $F_\mathrm{d} = (\rho_a U^2 L^2) \cdot \psi(\mathrm{Re})$, where U is the mean speed of the flow, L is the typical length scale of the bluff body, and $\mathrm{Re} = \rho_a U L/\mu_a$ is the Reynolds number, with ρ_a and μ_a the mass density and dynamic viscosity of the fluid (air in this case) [25]. In general, the functional dependence of the drag force on Reynolds number $\psi(\mathrm{Re})$ is not known *a priori*. For bluff bodies at moderate to high Reynolds numbers, however, it is known that the drag force is nearly independent of Re. For these conditions, $\psi(\mathrm{Re})$ can be taken as a constant, the drag coefficient C_d, and thus the drag force scales as $F_\mathrm{d} \propto U^2$ [26]. However, in a series of studies on leaves and other flexible objects exposed to a steady flow, it was shown that the possibility of reconfiguration can lead to drag reduction such that the exponent with which drag scales on U is reduced from the classic quadratic behavior, i.e., $F_\mathrm{d} \propto U^{2+\mathcal{V}}$, where $\mathcal{V} < 0$ [26,27]. This exponent is commonly referred to as the Vogel exponent. Different types of plants have been shown to be associated with different values of $\mathcal{V}$, in the range of $-1.3 < \mathcal{V} < -0.1$. The higher values of $\mathcal{V}$ occurred for tree branches, which is to be expected since they are closer to static bluff bodies [26].

In order to rationalize the appearance of Vogel exponents as a way to understand drag reduction caused by the reconfiguration of flexible bodies, several reduced models for loading configurations have been proposed. In these models the complex fluid-structure interaction which reconfigures the shape of the flexible body is modeled by a reduced loading force [28–31]. Pioneering approaches to this problem first used dimensional analysis to determine the theoretical Vogel exponent for bending of flexible beams and plates, to find $\mathcal{V} = -2/3$, which is in reasonably good agreement with experiments [24]. A similar argument has been used to predict $\mathcal{V}$ for flexible structures in the asymptotic regime of large deformations with respect to the typical length scale of the flexible body. Reference [20] coupled a simple model with experiments to determine the relation of the Cauchy number C_y (defined as the ratio of the force due to fluid loading on the plate to the bending rigidity of the plate per unit of length) to the Vogel exponent, as well as the extent of drag reduction. These experiments were performed using a wind tunnel where both rectangular specimens and disks cut in along several radii where exposed to flow at moderate to high Reynolds numbers $6400 \leqslant \mathrm{Re} \leqslant 54\,000$. Over this extensive range, the drag coefficient remained nearly constant for rigid bluff bodies. On the other hand, flexible objects, especially in the large-deformation regime, led to different Vogel exponents. The model in Ref. [20] showed that, for a rectangular plate, the streamlining effect on drag reduction is dominant for small deformations. For large deformations the effect of area reduction due to reconfiguration is more significant.

With an alternative point of departure, Refs. [19,32] have used free-streamline theory to address the coupling between hydrodynamic loading and elastic bending on a fiber, specifically to establish how the aerodynamic drag scales with the flow velocity during reconfiguration. To test this idea, experiments were performed on a glass fiber of length L and rigidity E supported at its midpoint while being exposed to a flowing soap film (thickness h) with uniform speed U. The underlying reduced equation for the beam curvature depended solely on one parameter, the nondimensional

speed $\eta = (\rho_f h L^3 U^2/2E)^{1/2}$, which can also be regarded as the ratio between the kinetic energy of the fluid and the elastic potential energy of the fiber. It was found that, for $\eta \ll 1$, the fiber remained nearly undeformed; C_d was constant and the dimensionless drag force $\tilde{F}_\mathrm{d}$ scaled quadratically with η, $\tilde{F}_\mathrm{d} \propto \eta^2$. For $\eta \gg 1$, the fibers took on a self-similar shape and $\tilde{F}_d \propto \eta^{4/3}$ [32]. This means that no reconfiguration is displayed by the flexible beam when $\eta \ll 1$ and thus $\mathcal{V} = 0$, whereas the $\eta \gg 1$ case leads to a Vogel exponent of $\mathcal{V} = -2/3$, as shown by this coupled elastohydrodynamic system.

A third, and arguably more standard, approach to generate a reduced model to describe the aeroelastic coupling is to explicitly include the reconfiguration effect on the normal loading pressure by dividing it into two terms. The first term is the local drag force acting in the same way as the drag acting on a perpendicular plate. The second term arises from the local acceleration of the flow on the deformed flexible body. This idea was first presented by Lighthill [31]. The combined action of these loading terms were applied recently for the deformation of flexible elastic sheets exposed to a uniform air flow [28]. In that study, sheets were laid flat and clamped on the downwind end of a wind tunnel. The air flow then caused the sheets to lift, bend, and accumulate such that the bunch of sheets eventually arrives at a steady state supported by the fluid loading. The model was used to successfully compute the shape of the sheets, using the drag coefficient as the only fitting parameter for a large range of wind speeds.

We commented above on how the flexibility of structures has a strong effect on the drag (due to reconfiguration), and so does the effect of porosity ϕ defined, for a slender perforated plate, as the volume fraction of material replaced by voids. In the limit of large Re, the effect of porosity has often been studied in relation to screens, which cause a reduction in pressure when used to obstruct flow [33]. Many investigations [33–41] have been done with both experimental measurements and theoretical modeling to examine the dependence of the drag coefficient on the pressure loss coefficient K rather than directly on ϕ. The pressure loss coefficient, when the incident flow is normal to the screen, has been historically defined as $K = \Delta p/\frac{1}{2}\rho_a U^2$, where Δp is the pressure difference across the screen. The value of K is known to be a function of ϕ, Re, and the Mach number Ma [33]. However, at large Re and low Ma, the pressure loss coefficient becomes only a function of ϕ, with past studies [39,41] proposing the relation $K \sim (1-\phi)/\phi^2$, where the proportionality constant is of order 1, similarly to the case of the drag coefficient in F [33,40,41].

Taylor [40] was one of the pioneers in describing the effect of porosity on the drag of a perforated screen. His modeling strategy was to replace the screen by a uniformly spaced array of sources. The flow field produced by combining the free-stream flow with the one generated by the resistance sources yielded a prediction for the drag coefficient of the screen as a function of the pressure loss coefficient [41]. This method proved to be reasonable for small values of K (large values of ϕ) where C_d decays to 0 with K, but failed at high values of K (low values of ϕ) where it predicted that C_d would decrease with increasing K. At high values of K, C_d should attain a constant value (the drag coefficient of the continuous sheet). In Ref. [37], a refinement of this prediction adapted the previous model to determine C_d as a function of K which produced a saturation of C_d up to a constant value with increasing K [37]. These predictions have been tested experimentally in several studies. Reference [34] measured the pressure loss and drag coefficients of perforated plates as a function of porosity and found reasonably good agreement with the above-described theoretical results, especially for large porosity. Later, Ref. [35] reported experimental results on perforated plates and measurements on the corresponding drag coefficients, using both the wake traverse method and a drag balance method. Similarly good agreement was found with the predictions of Ref. [37] and experimental results of Ref. [34] for high porosity but found worse agreement for low porosity.

While there have been numerous studies on independent effects of either porosity or flexibility on drag, there is a dearth of work that combines the two effects. A proxy to the effect of porosity on the drag coefficient of flexible structures has been studied in a reconfiguration experiment on what was called a poroelastic system, which involved experiments on spherical body with many flexible fibers extending radially outward [42]. It was found that the body as a whole had a Vogel exponent $\mathcal{V} = -1$ rather than the previously found $\mathcal{V} = -2/3$ for independent slender structures [42]. This study combined flexibility and porosity by using several independent flexible bodies placed in close

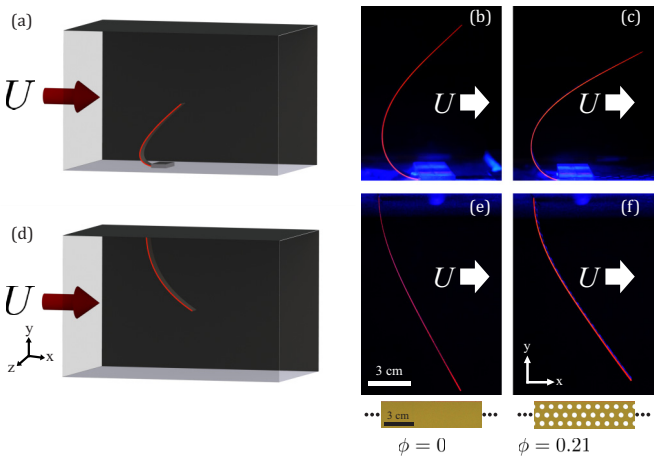

FIG. 1. (a)–(c) Horizontally clamped configuration. (d)–(f) Vertically clamped configuration. (a) and (d) Schematic diagram of the samples mounted in the wind tunnel. (b) and (c) Representative still images in a horizontally clamped configuration, each at $U = 9.8$ m/s. (e) and (f) Representative still images in a vertically clamped configuration, each at $U = 2.1$ m/s. (b) and (e) are the same sample with $\phi = 0$ and bending stiffness $B = 0.0125$ Nm. (c) and (f) are the same sample with $\phi = 0.21$ and $B = 0.006\,02$ Nm.

proximity to one another. More recently, a different study used numerical simulations to track the effect of porosity on the flapping dynamics of a one-dimensional filament exposed to axial flow. It was discovered that both the flapping amplitude and flapping frequency drop when the porosity is above a critical level [43]. There is a distinct lack of exploration on the combined effects of flexibility and porosity on the shape of statically deformed singular bodies in flow.

Here we investigate the effect of both flexibility and porosity on the aerodynamic drag of rectangular elastic strips that are exposed to a uniform air flow, at high-Reynolds-number conditions. We make use of a combination of wind tunnel experiments and computer simulations using a reduced model. Moreover, we consider elastic strips with different material properties, over a wide range of porosities. The strips were studied in two different experimental configurations (horizontal and vertical clamping), as described in Fig. 1. The deformed profile of these flexible perforated samples is experimentally measured and compared to the simulations. A restriction on the maximum deformation is imposed to validate the numerically generated profiles against experiments; namely, the maximum angle of deflection of the tip of the flexible strips is 45° with respect to the horizontal. Geometrically this means that, beyond this point, the tangential shear effects on drag are assumed to be no longer negligible. By comparing and fitting the experiments to the computed profiles, we measure the drag coefficient C_d as a function of porosity for different velocities, bending stiffnesses, and degrees of deformation. We found that the drag coefficient for perforated flexible strips decreased with increasing porosity, in a way that quantitatively parallels that of perforated rigid plates [34,35] for the horizontally clamped configuration but not for the vertical configuration. Unexpectedly, we have found that the drag coefficient values for the vertically clamped configuration are smaller than those of the horizontal configuration, except for the solid strips where they coincide. Using these data, we also study the effect of porosity on the deformation of perforated strips by computing the drag coefficient as a function of the Cauchy number. In that regard, we find that for a given value of porosity, the drag coefficient remains constant as a function of Cauchy number for a large range of material properties and flow speeds.

Our paper is outlined as follows. In Sec. II, we describe the experimental setup and measurement techniques used to acquire data, which are then compared to the reduced model presented in Sec. III. The experimental results on continuous strips (no porosity) are presented and discussed in Sec. IV. In Sec. V, we characterize the effect of porosity on the material properties of the strips, namely, mass

density and bending stiffness. After this characterization, the strips are exposed to wind loading. The results of this procedure are presented in Sec. VI. In Sec. VII, we present and analyze the discrepancies between our experimental results in different loading configurations. We provide a discussion and summary in Sec. VIII.

II. WIND TUNNEL EXPERIMENTS

For our experiments, we performed wind tunnel tests with flexible strips of different thicknesses and levels of porosity. Each strip was clamped to one of the walls of the test section of the horizontal wind tunnel such that the face of the strip was set perpendicular (and the thickness parallel) to the flow direction. We considered the two configurations shown in Figs. 1(a) and 1(d), with a strip that was either clamped vertically or horizontally and both cases exposed to horizontal flow, both of which will be described in detail below. For each strip, experiments were performed over a range of flow speeds. The deformed profile of the strip was measured by taking videos through a clear side wall of the test section of the wind tunnel. The sample strips were laser cut (Laser Pro, Spirit GLS) with width $w = 28$ mm, length $l = 275$ mm, and thickness $0.242 \leqslant h \leqslant 0.508$ mm from polyethylene terephthalate (PETG) or acetate sheets (mass densities $\rho \in [1280, 1330]\text{kg/m}^3$, respectively). One edge of each strip was painted fluorescent orange (Liquitex) to aid with the visualization and subsequent image processing.

Our experiments made use of an open return wind tunnel with a $100 \times 30.5 \times 30.5$ cm^3 test section capable of producing uniform steady flows with speeds in the range $2 < U < 34$ m/s, which are measured by a pitot tube and a high-accuracy capacitance manometer (690A Baratron, MKS Instruments). At the location of the clamps, the displacement thickness of the boundary layer is $\delta^* \approx 1.5$ mm. In comparison to the length of the strips, the boundary layer is therefore small (approximately 1%). As such, we believe that neglecting the nonuniformity in the oncoming flow due to the presence of the boundary layer is appropriate. For all the values of U used in this study, the fluctuations of the wind speed were below 1% of the mean velocity. There was no need to consider blockage corrections since the maximum blockage (defined as the ratio of the projected area of the strip normal to the flow to the cross section of the wind tunnel) was always below 5%. The flow direction was aligned with the x axis [see the definition of the axes in Fig. 1(d)]. The far-side wall and the ceiling (in the xy and xz planes, respectively) of the test section were painted matte black in order to block as much exterior light as possible, as well as minimize reflections. The near-side wall and floor (in the xy and xz planes, respectively) were made of optically clear acrylic, as shown in the schematics of Figs. 1(a) and 1(d). An array of black lights was placed beneath the floor of the test section to make the orange paint on the edge of the strips fluoresce. A camera (D3200, Nikon) was placed 1.5 m away from the test section of the wind tunnel such that the edge of the strips could be captured through the near-side transparent wall.

As noted above, two different configurations of the strips within the wind tunnel were studied. The first was similar to that of Ref. [28], albeit with a single strip in the current study, and will be referred to as the horizontally clamped configuration [see Figs. 1(a)–1(c)]. In this horizontally clamped case, the strip was placed flat at the center of the floor of the test section. An acrylic block was used to secure the downwind end of the strip to enforce a clamped boundary condition while being aligned with the direction of the flow. Upon clamping, the total length of the strip that was free to deform was $L = 152.4$ mm. Note that to obtain nontrivial (i.e., deformed) configurations of the strip, it was required that the flow speed be set above a critical value such that the aerodynamic loading could support the self-weight of the strip [28]. The second configuration considered, shown in Figs. 1(d)–1(f), will be referred as the vertically clamped configuration. In this case, the strips were exposed to the flow through a small slit on the ceiling of the test section, which also acted as a clamp by allowing the samples to be affixed vertically. To achieve this clamping, a section of the ceiling was set on a sliding track. In the open position, the strip could be inserted and the ceiling could then be closed onto the strip. Through the thickness of the ceiling, thin strips of latex (0.1 mm thick) were glued in place in order to tightly secure them. Directly using the ceiling as the clamp ensured that

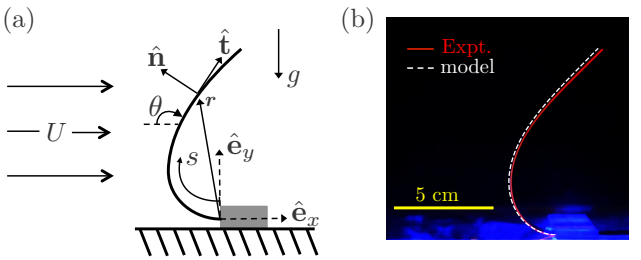

FIG. 2. (a) Diagram of the beam deformation. The local deflection angle $\theta(s)$ behaves according to Eq. (2). (b) Numerical solution to the forcing model (3) (dashed white line) overlaid atop a typical experimental observation (solid red line). The PETG strip shown has length $L = 15.24$ mm and bending stiffness $B = 0.0125$ Nm and was exposed to a wind load of $U = 9.8$ m/s.

the sample was clamped right at the point where it entered the wind tunnel and at a 90° angle with respect to top surface of the test section of the wind tunnel. Similarly to the horizontally clamped configuration, the total length of the clamped strip that was free to deform was $L = 152.4$ mm. In both configurations (horizontal and vertical clamping), the painted edge of the strip faced the near-side wall of the extension and thus the camera. Illumination was reduced within the wind tunnel facility such that the effect of the black light on the fluorescent paint on the edge of the strip enhanced the contrast between the sample and the background. This process greatly simplified the extraction of the deformed profile of the strips, in both the horizontal and the vertical configurations.

Each experiment was performed by first allowing the wind tunnel to reach a steady flow speed U whose value was recorded using the pitot tube. During the experiments, the strips were not perfectly steady but instead had small-amplitude unsteady oscillations. These oscillations are thought to be due to unsteadiness of the incoming flow rather than resulting from aeroelastic fluttering [1]. The amplitude of oscillations was small compared to the level of deflection of the entire strip (the amplitude of the tip oscillation was smaller than 2 mm). Because of these oscillations, a single still image might not have captured the equilibrium position of the strip, so videos were taken instead. Each video was 10 s long and taken at 24 frames/s. The equilibrium position of the strip for a given velocity was determined using a custom image processing algorithm. Representative examples of the experimental deformation profiles obtained after this image processing are provided in Fig. 3 below (solid lines).

III. MODEL

In Fig. 2(a) we present a schematic diagram of the geometry of the problem that we seek to model, along with the definition of several relevant quantities. To interpret the experimental data and rationalize the results, we use a reduced model based on the classic Kirchoff-Euler beam equations in the xy plane and take into account interaction between the elastic strip and the flow through an aerodynamic forcing term. In the absence of twist, and incurring uniform loading along the depth, the two-dimensional (in-plane) slender rod equations presented in Eqs. (1) below describe the large deformation of the elastic strips under aerodynamic loading. As derived in Ref. [44], by considering the forces and torques acting on a differential element of a beam of width w, height h, and length L, the local rate of change in linear and angular momentum, per unit length, and kinematics are

$$\rho_s w h \frac{\partial^2 \boldsymbol{r}}{\partial t^2} = \frac{\partial \boldsymbol{F}}{\partial s} + \boldsymbol{P} - (\rho_s g h w)\mathbf{e}_y, \tag{1a}$$

$$\frac{\rho_s w h^3}{12} \frac{\partial^2 \theta}{\partial t^2} = \frac{\partial M}{\partial s} + \boldsymbol{F} \cdot \hat{\mathbf{n}}, \tag{1b}$$

$$M = B w \frac{\partial \theta}{\partial s}. \tag{1c}$$

In the schematic diagram of Fig. 2(a), we sketch the definitions of important variables in our problem: the local deflection angle $\theta(s,t)$, which is a function of time t and arc length s; the local position vector $\boldsymbol{r}(s,t)$; the tangential vector $\hat{\mathbf{t}}$; and the normal vector $\hat{\mathbf{n}}$. Acting on the beam are the internal forces $\boldsymbol{F}(s,t)$, external load per unit length $\boldsymbol{P}(s,t)$ (and gravity), and internal moment $M(s,t)$. The material density of the strip is ρ_s and its bending stiffness is defined as $B = Eh^3/12(1-\nu^2)$ [45], where E is the Young modulus and ν is the Poisson ratio. Equation (1a) represents the local change in linear momentum due to the acting forces, Eq. (1b) represents changes in angular momentum due to moments about the local arc length s, and Eq. (1c) represents the local internal moment due to beam bending. Boundary conditions require $\theta = 0$ at the clamped end $s = 0$ in addition to the absence of internal force $\boldsymbol{F} = 0$ and moment $M = 0$ at the free end $s = L$. This last condition, when introduced into Eq. (1c), imposes the curvature restriction $\partial\theta/\partial s = 0$ at the free end.

In equilibrium, the fluid load acting on the strip balances its weight and the beam stands still in a deformed shape. Under these conditions, time derivatives vanish and Eq. (1) may be combined into the single nonlinear integro-differential equation

$$Bw\frac{d^2\theta}{ds^2} + \hat{\mathbf{n}} \cdot \int_s^L (\boldsymbol{P} - \rho_s g h w \hat{\mathbf{e}}_y) ds = 0, \tag{2}$$

where Eq. (1a) was integrated from s to L in order to satisfy the free-end boundary condition $\boldsymbol{F}(L,t) = 0$ for all values of t. Equation (2) can be solved once the external loading $\boldsymbol{P}$ is known. The challenge is that, in general, $\boldsymbol{P}$ is not known *a priori*. Drawing upon the work in Ref. [28], we chose to investigate the horizontal geometry shown in Figs. 1(a)–1(c) and 2, for which the following loading model has been introduced:

$$\begin{aligned} \boldsymbol{P} &= \frac{Bw}{L^3}\left(\frac{1}{2}C_d C_y \sin^2\theta - \frac{\pi}{4}\frac{w}{L}C_y \cos^2\theta \frac{d\theta}{ds}\right)\hat{\mathbf{n}}, \\ &= (P_d + P_l)\hat{\mathbf{n}}, \end{aligned} \tag{3}$$

where $C_y = \rho_a U^2 L^3/B$ is the Cauchy number (the dimensionless ratio between aerodynamic and bending forces) with ρ_a the air density. The first term P_d in Eq. (3) represents the local drag forces, arising from purely inertial effects, of a flow impinging perpendicular to the surface at each point $\boldsymbol{r}(s,t)$, i.e., $P_d \propto (U\hat{\mathbf{e}}_x \cdot \hat{\mathbf{n}})^2 = U^2 \sin^2\theta$. This term is characterized by a single fitting parameter C_d, the local drag coefficient that is taken as a global constant. Lighthill local forces due to momentum changes in the flow tangential to the beam arising from advection [31] are accounted for via the second term in Eq. (3) as

$$P_l = (U\hat{\mathbf{e}}_x \cdot \hat{\mathbf{t}})\frac{d}{ds}\left(\rho_a \pi \left(\frac{w}{2}\right)^2 (U\hat{\mathbf{e}}_x \cdot \hat{\mathbf{n}})\right) = -\rho_a \pi \left(\frac{w}{2}\right)^2 U^2 \cos^2\theta \frac{d\theta}{ds}. \tag{4}$$

The system described by Eqs. (2) and (3) is solved by a finite-difference method in which the local deflection in the forcing terms is initiated by a slight disturbance and then updated over each iteration until convergence between steps. In particular, computations are initialized with $\theta_0(s) = s/L$, which fixes $\boldsymbol{P}_0$ and $\hat{\mathbf{n}}_0$ in Eq. (3) for the first iteration.

Returning to Eq. (2) with the derivative operator replaced by the centered finite-difference matrix of 250 nodes in s, $[D^2]$, and enforcing boundary conditions, an updated curvature angle $\theta(s)^{(\text{new})}$ is obtained by matrix inversion

$$\theta(s)^{(\text{new})} = -\frac{1}{Bw}[D^2]^{-1}\left(\hat{\mathbf{n}}_0 \cdot \int_s^L (\boldsymbol{P}_0 - \rho_s g h w \hat{\mathbf{e}}_y) ds\right). \tag{5}$$

The boundary condition at the end of the strip ($s = L$) is $d\theta/ds = 0$. The other boundary condition at the clamping location ($s = 0$) is set such that the initial angle in the numerical simulations is equal to that measured in the experiments $\theta_0 = \theta_{0,\text{expt}}$, which is always less than 3°. Convergence is reached once repetitive application of the procedure above leads to less than 0.5% changes in $\theta(s)$.

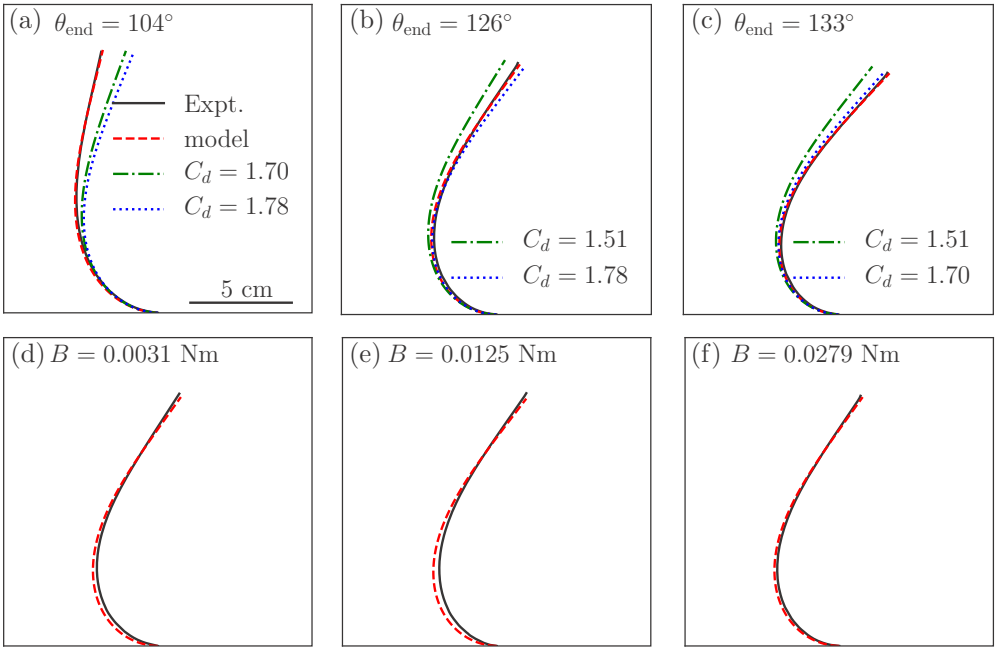

FIG. 3. Examples of fitting drag coefficient C_d in the model to the experiments. (a)–(c) For the same strip of bending stiffness $B = 0.0279$ Nm, the wind tunnel is set to exhaust air at velocities $U = 10.3$, 12.7, and 14.0 m/s, respectively, and fitted values for the drag coefficient are, respectively, $C_d = 1.51$, 1.70, and 1.78. The degree of deformation, given by the angle at the free end, is shown above each profile. For each tip deflection, profiles calculated with other values of C_d are also shown (dotted and dash-dotted curves). (d)–(f) For similar end deflections $\theta_{\text{end}} \approx 126°$, the bending stiffnesses are displayed for each material while exposed to wind velocities $U = 4.5$, 8.3, and 12.7 m/s, respectively, and the corresponding fitted values of $C_d = 1.71$, 1.84, and 1.70.

Finally, the arc profile of the beam is drawn by computing the local position through integration of the tangent vector

$$\boldsymbol{r}(s) = \int_0^s \hat{\mathbf{t}}\, ds, \tag{6}$$

as illustrated in Fig. 3 (dashed line) for different values of the bending stiffness of the strip and loading velocities. Comparisons of the beam profile produced from the model and captured from experiments are discussed in the following section.

The vertically clamped configuration [shown in Figs. 1(d)–1(f) and discussed in Sec. VII] can be readily described through the vertical analog of Eq. (3), by modifying the trigonometric factors accordingly. Namely, the transformation $\theta(s) \to -[\theta(s) + \pi/2]$ will be applied in the vertical configuration so that boundary conditions remain unchanged and positive angles θ represent deformation in the flow direction.

IV. VALIDATION OF THE MODEL

Different strip profiles can be obtained for different values of the flow velocity U by numerically solving Eqs. (2) and (3), with some initial guess for C_d. Towards validating our numerical simulations, these computed profiles can then be compared to those obtained from the experiments presented in Sec. II, for samples with varying thicknesses tested at different values of U.

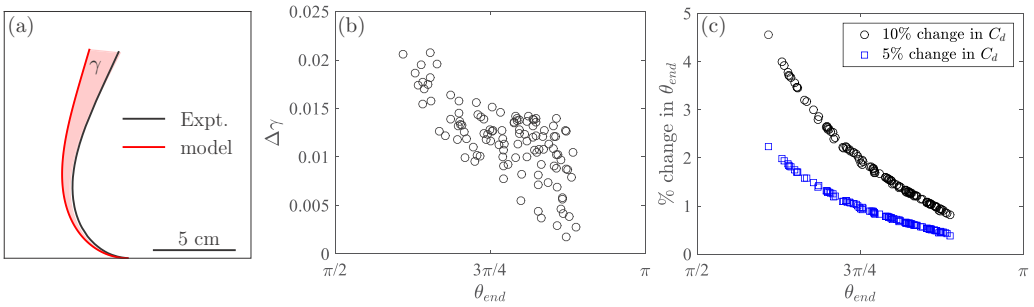

FIG. 4. (a) Experimental and numerical curves for $U = 12.7$ m/s and $B = 0.0279$ Nm with the area between the two curves shaded pink. The square root of the area between the two curves normalized by the beam length γ is minimized to find the best fit for C_d. (b) Plot of $\Delta\gamma$ as a function of the tip angle with respect to the horizontal θ_{end} for different porosity ϕ when the optimal C_d is changed by 10%. (c) Plot of θ_{end} percentage change as a function of θ_{end} for a 5% (□) and a 10% (○) change in C_d.

One way to compare the experimental and numerical profiles is to minimize the error per unit of arc length γ between the two curves (experimental and numerical) for each strip at a given velocity, i.e., the square root of the area between the two curves along the arc length normalized by the length L of the strip, as shown in Fig. 4(a). To minimize this error, Powell's optimization scheme is invoked to best adjust C_d. The results are visually inspected to verify that the outputs are valid, as shown in Fig. 2. Alternatively, one could have considered the objective of minimizing the difference in $\theta(s)$ generated from the computational procedure with that obtained by processing experimental profiles. However, by minimizing a function related to the area between numerical and experimental profiles, the error in C_d may be interpreted more directly as it leads to different computed values of θ_{end} in comparison to observations. As such, we chose to focus on γ.

The precision of the fitting procedure may be quantitatively evaluated by considering the change in γ as a function of other parameters. Having obtained the optimal fit of C_d for each experiment by minimizing γ of a given strip at fixed U, we then consider how deviations from the optimal C_d change the objective function γ to quantify the sensitivity of the fit. The corresponding differences in the objective function $\Delta\gamma$ are found by solving Eqs. (2) and (3) with a 10% increase and decrease in C_d. The average $\Delta\gamma$ from these two modified drag coefficients are plotted in Fig. 4(b) for each experiment, from which it appears that changes in C_d lead to a smaller change in $\Delta\gamma$ as the beam deformation increases. A way to easily quantify this deformation is to measure the angle at the free end of the strip θ_{end}. We can see in Fig. 4(b) that $\Delta\gamma$ decreases as θ_{end} increases. A physical interpretation can be drawn from the data shown in Fig. 4(c): Changing C_d leads to a change in tip deflection angle $\Delta\theta_{\text{end}}$. By modifying C_d to be 5% and 10% above and below the optimal fit and taking the average of the resulting difference in tip deflection from the two numerical solutions to Eqs. (2) and (3), we plot the predicted change $\Delta\theta_{\text{end}}$ as a function of θ_{end} obtained from the optimal fit of C_d to experiments. Visually, Figs. 3(a)–3(c) show this same effect. In the figure, the red dashed line corresponds to the profile calculated with the optimal C_d, whereas the blue dotted and green dash-dotted lines represent the profiles calculated with suboptimal C_d values (we used values corresponding the optimal C_d for the other two tip deflections shown in the figure). The profiles calculated by setting C_d slightly away from the optimal value lead to more pronounced differences from the optimal profiles at smaller tip deflections than at larger tip deflections, which is in agreement with the results shown in Figs. 4(b) and 4(c).

Taking the results of Figs. 4(b) and 4(c) in aggregate, it then becomes apparent that a clear systematic bias exists in favor of fitting C_d at lower deflections, where the drag coefficient can be fitted to more accurately. In other words, the computed profiles and the associated fitted values of C_d are less accurate for beams that are highly deformed. We speculate that this observation may be rationalized by considering the effects of aerodynamic shear drag on the elastic beam. Note that Eq. (3)

accounts solely for drag normal to the surface of the beam and neglects the tangential components of drag. In the regime of strong aerodynamic loading, as the static beam profile approaches the horizontal, enhanced skin friction is expected to act, in addition to the normal component of drag (due to a larger surface being aligned closer to the flow direction). Thus, the normal component of the drag may no longer be dominant and tangential stresses must also be taken into account. Since a modification of the aerodynamic loading model that accounts for shear is beyond the scope of our work, we restrict our analysis to bending profiles with a maximum tip deflection angle $\theta_{\text{end}}^{(\max)} = 135^\circ$ (i.e., 45° from the vertical). We recognize that our specific choice for the value $\theta_{\text{end}}^{(\max)}$ is not based on a formal argument but instead on our expectation that, below that threshold, normal aerodynamic forcing dominates and Eq. (3) is appropriate. For situations beyond $\theta_{\text{end}} > 135^\circ$, when the strip is highly deformed, we found that Eq. (3) was not a satisfactory model to describe our experimental data.

Next we illustrate our procedure of computing the shape of the aerodynamically loaded profiles and determining the associated C_d by fitting a series of experiments with various parameters. In Figs. 3(a)–3(c), the experimental and computed profiles correspond to the same elastic strip (zero porosity) at increasing values of the flow velocity: $U = \{10.3, 12.7, 14.0\}$ m/s, respectively. The black lines show the profiles extracted from experiments and the dotted red lines are results of the optimized numerical fit. The corresponding drag coefficients (computed through fitting) $C_d = \{1.51, 1.70, 1.78\}$ appear to vary slightly with overall curvature, slightly increasing with deformation. Along the bottom row in Fig. 3, continuous strips (no porosity) of three different bending stiffnesses are exposed to wind velocities ($U = \{4.5, 8.3, 12.7\}$ m/s, respectively) such that the end deflections are kept nearly constant at $\theta_{\text{end}} \sim 126^\circ$, i.e., to target three similar final configurations. The corresponding values of drag coefficient for these nearly identical deformed configurations are, respectively, $C_d = \{1.71, 1.84, 1.70\}$, only showing relatively small variations. On the other hand, for fixed strip properties or fixed velocities, variations in C_d are dominated by variations in θ_{end}. This issue of relating the fitted drag coefficient C_d and deformation (in terms of the Cauchy number C_y, the nondimensional loading parameter) will be discussed further in Sec. IV.

Taking the mean and standard deviation of the fitted drag coefficient over a set of nine experiments ranging in bending stiffness $B = \{0.0031, 0.0125, 0.0279\}$ Nm and velocities $3.9 < U < 14.0$ m/s, we have found that our continuous strips (without any perforations) have $C_d = 1.68 \pm 0.21$, in agreement with Ref. [28].

V. CHARACTERIZATION OF THE STRIPS: BENDING STIFFNESS VS POROSITY

The central emphasis of the present study is to quantify how the level of porosity of a slender flexible strip affects its aerodynamic loading and, consequently, its extent of deformation. To systematically study porosity as a parameter, we laser cut a hexagonal array of circles of radius r on either solid PETG or acetate strips, as described in Sec. II. Care was taken during the cutting procedure to avoid warping of the strip due to excessive heating, which may induce local volume changes near the edges of the cut, thus changing the homogeneity of the thickness of the strip and modifying its flexural properties. The distance between the centers of the circles in the hexagonal lattice was 5.1 mm, which was fixed for all samples. A representative design of the laser-cut layout is shown in Fig. 5(a). This hexagonal arrangement of holes is identical to that of Ref. [35]. The porosity ϕ is defined as the ratio between the area of all the holes to the total bounding area of the strip. The explored levels of porosity were in the range $0 \leqslant \phi \leqslant 0.68$, changed by modifying r while keeping all other parameters of the layout constant. Examples of samples with different levels of ϕ are shown in Fig. 5(b).

The bending stiffness for each strip (with different levels of porosity) was measured by horizontally clamping it as a cantilever beam and quantifying the deformation that ensues due to self-weight. Images of the deformed strips were acquired and processed using the same procedure described in Sec. II. The cantilever (hanging) length of the strip was set to $L = 15.24$, 20, and 25 cm. For $L = 15.24$ cm the strip was secured such that the clamp bisected a hole in the center column of the

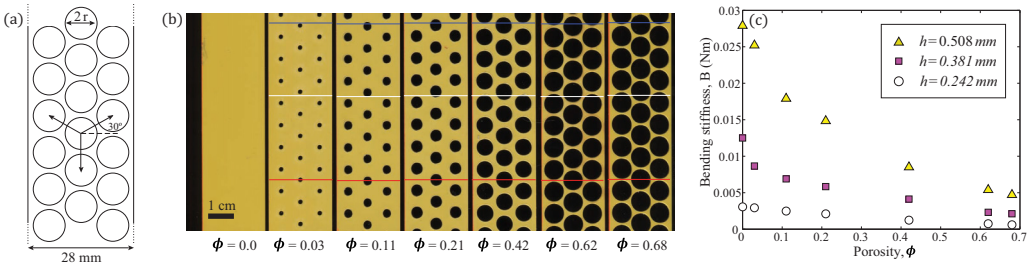

FIG. 5. (a) Schematic of the strips containing a hexagonal arrangement of voids, with a level of porosity of $\phi = 0.62$. (b) Strip samples of PETG ($h = 0.508$ mm) for increasing porosity ϕ from 0 to 0.68. (c) Bending stiffness B as a function of ϕ for $h = 0.242$ mm (○), 0.381 mm (□), and 0.508 mm (△).

strips, as shown by the red line in Fig. 5(b). This is the same position where the strips were clamped during the wind tunnel experiments. For $L = 20$ and 25 cm, the strips were clamped through different regions of the unit cell, as indicated by the white and blue lines, respectively, in Fig. 5(b). For each value of L, a bending stiffness B was found following a procedure similar to the one used above to compute C_d. With only gravity acting as an external force, Eq. (2) reduces to

$$B\frac{d^2\theta}{ds^2} - \rho_s g h(1-\phi)(L-s)\cos\theta = 0, \tag{7}$$

where the parameters ρ_s, h, L, and ϕ are known *a priori* and B is the only unknown. This classic model is well known to work for solid continuous beams ($\phi = 0$) and when the mass of the strip is evenly distributed as a uniform density ρ_s. To extend the model to the perforated strips, the same assumption was made. However, since the mass is less due to the addition of the holes, an effective density with value of $\rho_s(1-\phi)$ was also assumed to be uniform throughout the strip. With this effective density, the strips are then treated as if they were otherwise continuous. Solving Eq. (7) for some initial guess of B, the resulting deflection is first compared to experimental measurements. The area between the experimental and numerical curves is then minimized with respect to the bending stiffness B. In Fig. 5(c) we present results for the obtained values of B as a function of ϕ, for different thickness values ($h = \{0.242, 0.382, 0.508\}$ mm). For each strip, we found that the measurements of the resulting bending stiffness varied at most by 3.4%, regardless of the length and the specifics of the clamping position. As expected, the bending stiffness is larger for larger values of h, since $B \propto h^3$, and decreases with ϕ for every thickness h. Below we will use the above results as a reference when requiring knowledge about the relation of B as a function of ϕ.

VI. DRAG COEFFICIENT OF PERFORATED ELASTIC STRIPS

Wind tunnel experiments were performed using the perforated strips described above (Sec. V), following a protocol identical to that for continuous strips (Sec. IV), in both the horizontally and the vertically clamped configurations. By fitting the experimental and the numerical profiles (Sec. IV), the drag coefficient C_d was then computed for different values of porosity ϕ, bending stiffness B, and flow speed U. An important point here is the assumption that the same treatment used for continuous strips can be applied to the loading of perforated strips, following Eq. (1). This means that the perforated strips are treated as if they are solid strips with an area equal to $L \times w$ and with a value for the bending stiffness B that was measured in Sec. V.

For each specimen, experiments were run at several different values of the flow speed U and the experimental data were used to numerically compute the corresponding values of the drag coefficients C_d. These individual C_d values calculated for each level of porosity were then averaged over the range of U to yield a single C_d for each level of porosity ϕ. In Fig. 6, we plot the averaged drag coefficient as a function of the porosity obtained from our experiments on flexible perforated strips

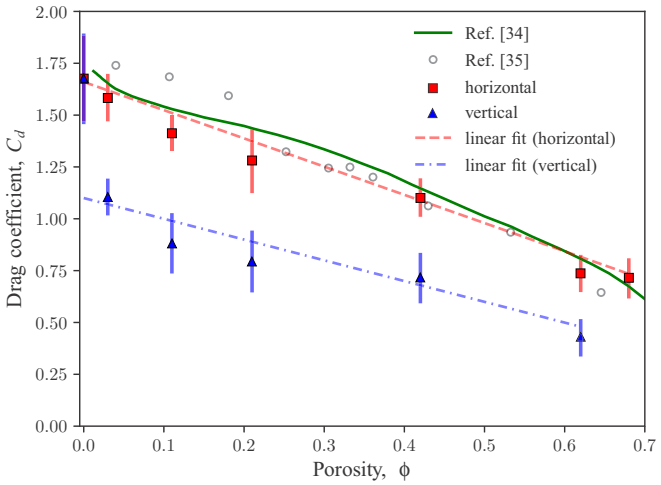

FIG. 6. Drag coefficient C_d as a function of porosity ϕ. The solid green line shows experimental measurements extracted from Ref. [34] and open circles are experimental measurements extracted from Ref. [35], both for rigid perforated plates. Closed red squares (blue triangles) are the fitted C_d in the horizontally (vertically) clamped strip configurations. The dashed red line is a linear fit to all of the experimental data in the horizontal configuration and the dash-dotted blue line is the linear fit for the experimental data in the vertical configuration, excluding the case of $\phi = 0$.

in both configurations (horizontally and vertically clamped). Previous results from the literature for rigid perforated plates are also superposed on the plot [34,35].

First, let us focus on the horizontally clamped configuration. We find that the average C_d decreases monotonically with increasing ϕ from $C_d = 1.68 \pm 0.21$ (the value found in Sec. IV for continuous strips) down to $C_d = 0.71 \pm 0.10$ for $\phi = 0.68$. This trend is supported by the literature, specifically for rigid wire gauzes and screens [33,38,40]. In Fig. 6, the red squares are our experimental results of the horizontally clamped configuration and the solid triangles are results using the vertically clamped configuration. Each point represents the average of five to ten experiments. The error bars of both experimental data sets are the standard deviation of the averaging over velocity. The open circles are experimental measurements of C_d previously reported by Ref. [35] on wind tunnel experiments using the drag balance method for rigid perforated plates, with the same arrangement of holes as our samples. The green line are the results from Ref. [34]. Interestingly, and surprisingly to us, there is good agreement between the results for rigid plates from the existing literature [33–35,37,40,41] and our experimental data for flexible strips in the horizontal configuration, especially for large ϕ. There is some disagreement when $\phi < 20\%$: Our experimental values of C_d are 12%–15% lower than the data of Ref. [35] and 2%–5% lower than the prediction of Ref. [34] for rigid plates.

For the vertically clamped configuration, C_d also decreases with ϕ. However, we were surprised to find that, and do not yet understand why, these results differ significantly from those for the horizontally clamped cased discussed above, as well as from the previous data for perforated rigid plates [35] and the associated prediction [34]. We will discuss the vertically clamped configuration in more detail below (Sec. VII).

In order to quantify the effect of the wind loading on the extent of deformation of the flexible perforated strips, we first study the dependence on the computed (fitted) C_d on the free-stream velocity in the horizontal configuration for different values of ϕ, B, and h, as shown in Fig. 7. Each symbol in the plot represents a different level of porosity (in the range $0 \leqslant \phi \leqslant 0.68$). As shown above, the average C_d decreases with the porosity. However, there is no trend of the drag coefficient with the velocity. Due to the highly deformable nature of these structures, the characteristic length that would generally be used to define a Reynolds number is not trivial to determine. Given that in the

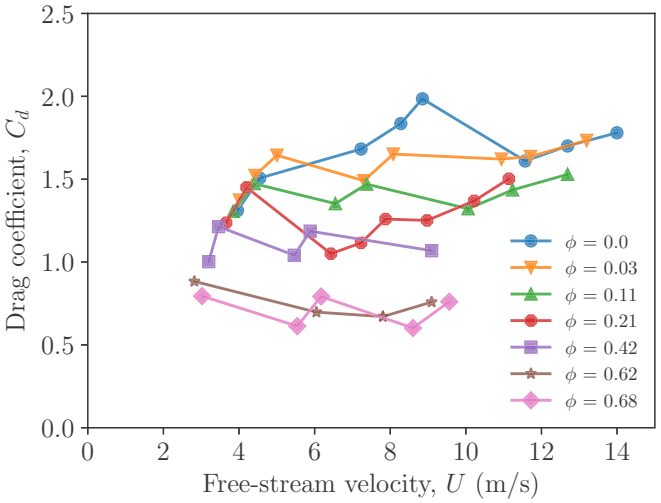

FIG. 7. Drag coefficient C_d as a function of the free-stream velocity U for different different levels of porosity $0 \leqslant \phi \leqslant 0.68$ in the horizontal configuration.

figure each curve is made up of experimental points with the same ϕ but various B, a dimensionless quantity that normalizes the fluid loading by a quantity that relates to the bending is appropriate to examine. Therefore, we proceed by nondimensionalizing the fluid loading by using the Cauchy number $C_y = \rho_a U^2 L^3 / B$.

In Fig. 8(a) we present a plot for C_d as a function of C_y for different values of ϕ, B, and h. The colors represent different wind velocities during the experiments. The black line of open symbols represents the average value of C_d over different values of the flow speed and bending stiffnesses for a given porosity ϕ. As shown in Figs. 6 and 8(a), the velocity-averaged value of C_d decreases with porosity ϕ. Fluctuations from these average values are below 10% and decreasing for increasing porosity. Then, for a given value of ϕ, the drag coefficient does not change as the perforated strips deform due to wind loading.

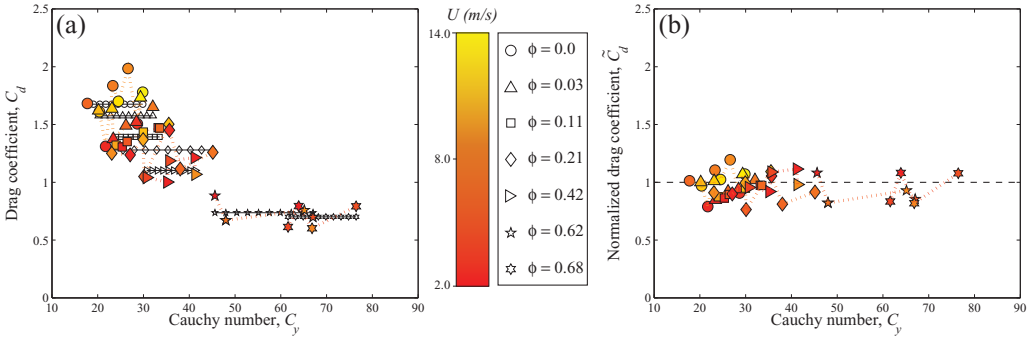

FIG. 8. (a) Drag coefficient C_d as a function of the Cauchy number $C_y = \rho_a U^2 L^3 / B$ for different porosity ϕ in the horizontal configuration. Horizontal symbol lines display average values of C_d for a given ϕ. (b) Normalized drag coefficient $\tilde{C}_d = C_d / C_0(1 - \alpha\phi)$ as a function of the Cauchy number $C_y = \rho_a U^2 L^3 / B$ for the same values of porosity ϕ in the horizontal configuration. The fitted parameters are $C_0 = 1.68$ and $\alpha = 0.82$. The color bar displays U in m/s.

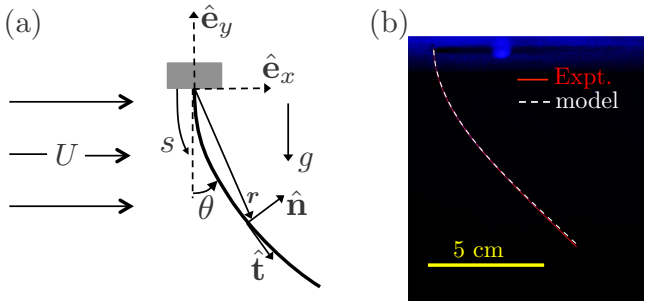

FIG. 9. (a) Diagram of the beam deformation hanging vertically. The local deflection angle $\theta(s)$, now measured from the vertical, behaves according to Eq. (2). (b) Numerical solution to the forcing model (8) (dashed white line) overlaid atop a typical experimental observation (solid red line).

Next, leveraging the monotonic decrease of C_d as a function of ϕ that we obtained in Fig. 6, we empirically fit C_d to the linear function $C_d^{\text{fit}} = C_0(1 - \alpha\phi)$, with $C_0 = 1.68 \pm 0.21$ (the value of C_d at $\phi = 0$) and $\alpha = 0.82 \pm 0.02$, where $C_0\alpha$ is the slope of the linear fit. It should be noted that other dependences of C_d on ϕ have been formulated. For example, the theory for screens in Ref. [40] (which diverges at $\phi = 0$) and its refinement by Ref. [37] (which saturates at $\phi = 0$) both yield a nonlinear dependence of C_d on ϕ. Here, for simplicity, we have decided to use a simple linear fit, which we then use to plot, in Fig. 8(b), the normalized drag coefficient $\tilde{C}_d = C_d/C_d^{\text{fit}}$ as a function of C_y for different values of porosity ϕ. The dashed line corresponds to $C_d \equiv C_d^{\text{fit}}$. We find a very good collapse of our data around $\tilde{C}_d = 1$ for all values of C_y. The variations of the data about $\tilde{C}_d = 1$ are below 10% for all perforated flexible strips and within 20% for the continuous strips.

Thus, in this configuration of horizontal clamping, the drag coefficient for flexible perforated strips decreases with porosity, in a fashion very similar to the one known and predicted for rigid plates. Using this observation, the drag coefficient can be rescaled to show that, when sorted by porosity, the drag coefficient is independent of the Cauchy number. Our empirical treatment of the data still leaves the fitted quantity α unexplained, but we hope that these results will instigate future theoretical work on this topic to help rationalize α.

VII. VERTICAL CONFIGURATION

We now turn our attention to a more detailed discussion of the case where the elastic strip is clamped vertically, which was already introduced in Figs. 1(d)–1(f). As described above, presuming the loading assumptions of Eq. (3), the modifications from the previous horizontal clamped cased to the current vertical case are purely trigonometric, $\theta(s) \to -[\theta(s) + \pi/2]$, such that the external aerodynamic loading can be written as

$$\boldsymbol{P} = \frac{Bw}{L^3}\left\{\frac{1}{2}C_d C_y \cos^2\theta - \frac{\pi}{4}\frac{w}{L}C_y \sin^2\theta \frac{d\theta}{ds}\right\}\hat{\mathbf{n}}, \tag{8}$$

where θ now measures the beam angle from the vertical (see Fig. 9). Our imposed restriction at the free-end now reads $\theta_{\text{end}} < 45^\circ$ and it is enforced to avoid scenarios in which tangential forces become increasingly important, following the same arguments used in the horizontal configuration (see Sec. IV).

Repeating the experimental and numerical procedures outlined above, the effects of porosity for this vertically clamped configuration are summarized in Fig. 6. The measured drag coefficient in this configuration decreases with porosity, in a way that is qualitatively similar to the one measured in the horizontal configuration. The fluctuations (error bars) around the mean values of C_d for every value of ϕ are of the same order as those of the horizontal case. However, the measured values of the

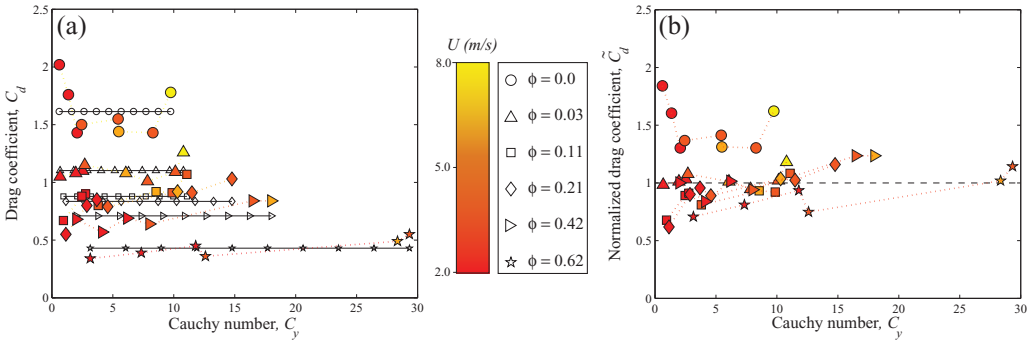

FIG. 10. (a) Drag coefficient C_d as a function of the Cauchy number $C_y = \rho_a U^2 L^3/B$ for different porosity ϕ in the vertical configuration. Horizontal symbols lines display average values of C_d for a given ϕ. (b) Normalized drag coefficient $\tilde{C}_d = C_d/C_0(1-\alpha\phi)$ as a function of the Cauchy number $C_y = \rho_a U^2 L^3/B$ for the same values of porosity ϕ in the vertical configuration. Here $C_0 = 1.10$ and $\alpha = 0.903$. The adjacent color bar displays U in m/s.

drag coefficient for strips with porosity are significantly lower (by 30%–35%) than the horizontally clamped results. This is not the case for the continuous strips, where they do arrive at the same value C_0 of the horizontally clamped case.

The fact that there is a quantitative difference between the values of C_d as a function of ϕ for both configurations is remarkable. These simple experimental configurations rely on the same type of loading, material or geometric properties for the strips, and levels of porosity; the only difference is the way they are clamped. This would mean that there is a strong dependence on boundary conditions for drag (and therefore on reconfiguration) when applied to flexible porous bodies. These effects appear to have been overlooked in the past and should be regarded in more detail in the future.

When C_d is computed as a function of C_y, shown in Fig. 10(a), the data for the vertically clamped case follow a trend similar to the horizontal case presented above. This means that C_d remains constant for different values of C_y when sorted by porosity. Following the same procedure as in Sec. VI, we linearly fit C_d as a function of ϕ (excluding the case of $\phi = 0$): $C_d^{\text{fit}} = C_0(1-\alpha\phi)$. The fitted parameters are $C_0 = 1.10 \pm 0.1$ and $\alpha = 0.93 \pm 0.03$, where $C_0\alpha$ is the slope of the linear fit. Using this fit, we plot in Fig. 10(b) the normalized drag coefficient $\tilde{C}_d = C_d/C_d^{\text{fit}}$ as a function of C_y for $\phi > 0$. The dashed line corresponds to the $C_d \equiv C_d^{\text{fit}}$. As in the case of the horizontally clamped perforated strips, we find a good collapse of all our data around $\tilde{C}_d = 1$ for all values of C_y, with variations below 15% for all values of $\phi > 0$.

There is a significant difference in the value of C_d between the case of continuous strips ($\phi = 0$) and the porous strips ($\phi > 0$) in this vertically clamped configuration. At $\phi = 0$, the mean value of the experimental data agrees well with the horizontally clamped configuration (within error bars) but it is 50% larger than the C_0 obtained from the linear fit for the vertical configuration, i.e., there is a sharp change as soon as some perforation is included ($\phi = 0.03$). Such a steep drop in the value C_d as a function of ϕ in the limit of small porosity is surprising and deserves further attention in future studies.

VIII. DISCUSSION AND CONCLUSION

We have presented results of an experimental and numerical study of the dependence of the drag coefficient C_d on porosity ϕ of flexible reconfigurable structures subjected to an aerodynamic loading in two different configurations (termed horizontal and vertical). In our current case of flexible strips we investigated the effect of flexibility on the drag force acting on perforated structures. It is widely known that an aeroelastic coupling between flow and structure leads to reconfiguration [24,26–28], which on its own presents challenges in their understanding. One of these challenges is to describe

the degree of deformation of elastic structures using reduced models which account for the complex fluid-structure interactions in different configurations.

In our present study we acquired and analyzed experimental data for the deformed shapes of porous elastic strips, for different values of U, ϕ, and B using the reduced model presented in Ref. [28], where C_d is the only global fitting parameter. We have found that C_d monotonically decreases with ϕ in both configurations. This tendency can be fitted accurately by a linear function on both the horizontal and vertical configurations for $\phi > 0$, as shown in Fig. 6, with different slopes and values at $\phi = 0$.

The observed decreasing trend of C_d as a function of ϕ for flexible perforated strips on both configurations resembles qualitatively what has been found for rigid perforated plates or screens for both clamping configurations. In these rigid counterparts, the dependence of C_d on ϕ has been an extensive subject of study in the literature via the pressure drop coefficient K. Since Refs. [40,41], several functional forms for K (and thus C_d) as a function of ϕ have been proposed and experimentally tested on rigid perforated screens and plates, and gauzes for large values of Re [35,38]. The main commonality across all these various studies is that the aerodynamic loading on these rigid structures can be tailored by increasing their porosity. This is also the case for our experimental study of perforated flexible structures in both configurations. In the case of the horizontal configuration, the drag coefficient for flexible perforated structures follows quantitatively the theoretical prediction for rigid plates (within error bars) [35]. We have also found that C_d is constant as a function of the Cauchy number C_y, which is the ratio between the force due to fluid loading on the elastic strip to its bending rigidity, for a given value of ϕ as displayed in Figs. 8(a) and 10(a). This relation is found for all our experimental values of flow speeds, material properties, and levels of porosity. Thus, we can argue that drag forces, when rescaled by porosity, are independent of the degree of reconfiguration of the flexible perforated strips, which we believe is an important finding from our work. As such, we have quantified the effect of porosity on the drag force on flexible structures upon wind loading.

It is important to highlight the fact that we have made use of a particular reduced model to describe our experimental data (and to compute C_d as a function of ϕ). While using our chosen model, we determined a value of C_d, which was defined as the local drag coefficient of an infinitesimal element of the strip. In doing so, it was implicitly assumed that this C_d is constant over the extent of the strip. This local drag coefficient is different from that of other reduced models, which often employ a more global definition of C_d, thereby allowing for claims about the Vogel exponent. In our work, we cannot comment on the appropriate Vogel exponent because we do not measure nor do we calculate the x component of the drag forces that would be required to determine the classical drag coefficient defined as $C_d = 2F/\rho U^2 A$. Reduced models such as the ones presented in Refs. [19,20,28,32,42,43] are used to describe the aeroelastically induced reconfiguration of elastic materials. The choice of each of these particular models depend strongly on the loading configuration of the system under study and that affects the way some of its properties are computed or measured. This poses a great challenge on the prediction and control of the shape of these flexible structures as they reconfigure when aerodynamically loaded. A more thorough study on the way reduced models are used on different configurations is needed. For instance, a first step could be the usage of different models on the same configuration, where a comparison of their predictive capabilities and differences can be made.

In the present work, we examined two configurations which were both clamped at the wall of the wind tunnel. The boundary layer thickness is small relative to the length of the strip ($\approx$1%) and thus unlikely to introduce nonuniform loading. However, the clamping near the wall could still affect the results, since the wall prevents the flow from traveling around the clamped end. We hope that our results will motivate future experiments, in both the horizontal and vertical configurations, where the strips are clamped across the center of the wind tunnel, away from the walls, similar to those experiments performed by Ref. [46]. These results could illuminate the reasons for the different results in our vertical and horizontal configurations, which we find intriguing, puzzling, and certainly worthy of further investigation.

In our study, we have taken a first step in studying the effect of a particular choice of reduced models on the predictability and control of drag and reconfiguration of flexible porous structures by

using the same reduced model on two different configurations. Although we have found qualitative agreement on the dependence of C_d on ϕ and C_y, there is a quantitative difference on the values of C_d as a function of ϕ between the horizontal and vertical configurations. This is a highly surprising puzzle which arises from the experimental data: Why would two configurations present distinctive drag coefficients when loaded in the same manner? Does the drag coefficient (and thus the Cauchy number) depend strongly on boundary (clamping) conditions of porous reconfigurable structures? Would other reduced models display the same problems? If so, is there a way to foresee why? We hope these unanswered questions, raised by the present study, will motivate further theoretical, experimental, and computational work in the future.

ACKNOWLEDGMENTS

This research was conducted with government support under and awarded by the Department of Defense (DoD) through the National Defense Science & Engineering Graduate Fellowship (NDSEG) Program, and by the National Science Foundation (CAREER Grant No. CMMI-1351449).

[1] M. P. Païdoussis, S. J. Price, and E. de Langre, *Fluid-Structure Interactions: Cross-Flow-Induced Instabilities*, 1st ed. (Cambridge University Press, Cambridge, 2014).
[2] D. S. Barrett, M. S. Triantafyllou, D. K. P. Yue, M. A. Grosenbaugh, and M. J. Wolfgang, Drag reduction in fish-like locomotion, J. Fluid Mech. **392**, 183 (1999).
[3] Y. Watanabe, S. Suzuki, M. Sugihara, and Y. Sueoka, An experimental study of paper flutter, J. Fluid. Struct. **16**, 529 (2002).
[4] R. H. Scanlan and J. J. Tomko, Airfoil and bridge deck flutter derivatives, J. Eng. Mech. **97**, 1717 (1971).
[5] R. H. Scanlan, The action of flexible bridges under wind, I: Flutter theory, J. Sound Vib. **60**, 187 (1978).
[6] R. H. Scanlan, in *Proceedings of the IAHR-IUTAM Symposium, Karlsruhe, 1979*, edited by E. Naudascher and D. Rockwell (Springer, New York, 1979), paper FI, p. 595.
[7] F. Bleich, Dynamic instability of truss-stiffened suspension bridges under wind action, Trans. Am. Soc. Civil Eng. **114**, 1177 (1949).
[8] Y. Rocard, *Dynamic Instability*, 1st ed. (Crossby Lockwood, London, 1957).
[9] N. Elvin, H. D. Akaydin, and Y. Andreopoulos, Flapping states of a flag in an inviscid fluid: Bistability and the transition to chaos, J. Intell. Mater. Syst. Struct. **21**, 1263 (2010).
[10] S. C. Mann, B. P. Dunnmon, J. A. Stanton, and E. H. Dowell, Power extraction from aeroelastic limit cycles, J. Fluid. Struct. **27**, 1182 (2011).
[11] L. Zhao and Y. Yang, Enhanced aeroelastic energy harvesting with a beam stiffener, Smart Mater. Struct. **24**, 032001 (2015).
[12] Y. Kim and C. S. Peskin, 2-D parachute simulation by the immersed boundary method, SIAM J. Sci. Comput. **28**, 2294 (2006).
[13] C. Eloy, C. Souilliez, and L. Schouveiler, Flutter of a rectangular plate, J. Fluid. Struct. **23**, 904 (2007).
[14] C. Eloy, R. Lagrange, C. Souilliez, and L. Schouveiler, Aeroelastic instability of cantilevered flexible plates in uniform flow, J. Fluid Mech. **611**, 97 (2008).
[15] S. Taneda, Waving motions of flags, J. Phys. Soc. Jpn. **24**, 392 (1968).
[16] W. Shyy, H. Aono, S. K. Chimakurthi, P. Trizila, C. K. Kang, C. E. S. Cesnik, and H. Liu, Recent progress in flapping wing aerodynamics and aeroelasticity, Prog. Aerosp. Sci. **46**, 284 (2010).
[17] E. H. Dowell and K. C. Hall, Modeling of fluid-structure interaction, Annu. Rev. Fluid Mech. **33**, 445 (2001).
[18] P. G. Reinhall, A. L. Eberle, and T. L Daniel, Fluid-structure interaction in compliant insect wings, Bioinspir. Biomim. **9**, 025005 (2014).

[19] S. Alben, M. Shelley, and J. Zhang, How flexibility induces streamlining in a two-dimensional flow, Phys. Fluids **16**, 1694 (2004).
[20] F. Gosselin, E. de Langre, and B. Machado-Almeida, Drag reduction of flexible plates by reconfiguration, J. Fluid Mech. **650**, 319 (2010).
[21] B. Bhushan and Y. C. Jung, Natural and biomimetic artificial surfaces for superhydrophobicity, self-cleaning, low adhesion, and drag reduction, Prog. Mater. Sci. **56**, 1 (2011).
[22] D. Terwagne, M. Brojan, and P. M. Reis, Smart morphable surfaces for aerodynamic drag control, Adv. Mater. **26**, 6608 (2014).
[23] A. Santhanakrishnan, A. K. Robinson, S. Jones, A. A. Low, S. Gadi, T. L. Hedrick, and L. A. Miller, Clap and fling mechanism with interacting porous wings in tiny insect flight, J. Exp. Biol. **217**, 3898 (2014).
[24] E. De Langre, A. Gutierrez, and J. Cossé, On the scaling of drag reduction by reconfiguration in plants, C. R. Mec. **340**, 35 (2012).
[25] L. D. Landau and E. M. Lifshitz, *Fluid Mechanics*, 3rd ed., Course of Theoretical Physics Vol. 6 (Pergamon, Oxford, 1987).
[26] S. Vogel, Drag and flexibility in sessile organisms, Am. Zool. **24**, 37 (1984).
[27] S. Vogel, Drag and reconfiguration of broad leaves in high winds, J. Exp. Bot. **40**, 941 (1989).
[28] P. Buchak, C. Eloy, and P. M. Reis, The Clapping Book: Wind-Driven Oscillations in a Stack of Elastic Sheets, Phys. Rev. Lett. **105**, 194301 (2010).
[29] L. Schouveiler, C. Eloy, and P. Le Gal, Flow-induced vibrations of high mass ratio flexible filaments freely hanging in a flow, Phys. Fluids **17**, 047104 (2005).
[30] S. Alben and M. J. Shelley, Flapping States of a Flag in an Inviscid Fluid: Bistability and the Transition to Chaos, Phys. Rev. Lett. **100**, 074301 (2008).
[31] M. J. Lighthill, Note on the swimming of slender fish, J. Fluid Mech. **9**, 305 (1960).
[32] S. Alben, M. Shelley, and J. Zhang, Drag reduction through self-similar bending of a flexible body, Nature (London) **420**, 479 (2002).
[33] E. M. Laws and J. L. Livesey, Flow through screens, Annu. Rev. Fluid Mech. **10**, 247 (1978).
[34] R. H. Blockley, M.Sc. thesis, University of London, 1968.
[35] I. P. Castro, Wake characteristics of two-dimensional perforated plates normal to an air-stream, J. Fluid Mech. **46**, 599 (1971).
[36] J. M. R. Graham, Turbulent flow past a porous plate, J. Fluid Mech. **73**, 565 (1976).
[37] J.-K. Koo and D. F. James, Fluid flow around and through a screen, J. Fluid Mech. **60**, 513 (1973).
[38] R. A. Pinker and M. V. Herbert, Pressure loss associated with compressible flow through square-mesh wire gauzes, J. Mech. Eng. Sci. **9**, 11 (1978).
[39] A. J. Reynolds, Flow deflection by gauze screens, J. Mech. Eng. Sci. **11**, 290 (1969).
[40] G. I. Taylor, Air resistance of a flat plate of very porous material, Aeronautical Research Council Report No. 2236, 1944 (unpublished).
[41] G. I. Taylor and R. M. Davies, The aerodynamics of porous sheets, Aeronautical Research Council Report No. 2237, 1944 (unpublished).
[42] F. P. Gosselin and E. De Langre, Drag reduction by reconfiguration of a poroelastic system, J. Fluid. Struct. **27**, 1111 (2011).
[43] D. Natali, J. O. Pralits, A. Mazzino, and S. Bagheri, Stabilizing effect of porosity on a flapping filament, J. Fluid. Struct. **61**, 362 (2016).
[44] B. Audoly and Y. Pomeau, *Elasticity and Geometry*, 1st ed. (Oxford University Press, Oxford, 2010).
[45] L. D. Landau, L. P. Pitaevskii, A. M. Kosevich, and E. M. Lifshitz, *Theory of Elasticity*, 3rd ed., Course of Theoretical Physics Vol. 7 (Pergamon, Oxford, 1986).
[46] D. Kim, J. Cossé, C. H. Cerdeira, and M. Gharib, Flapping dynamics of an inverted flag, J. Fluid Mech. **736**, R1 (2013).